Integrating a Localized B0 Shim Array into a Solenoid Transmit-Receive Coil for Permanent Magnet Scanners

Celine Veys
Rafael Calleja
Michael Lustig

Electrical Engineering and Computer Sciences
University of California, Berkeley

May 14, 2021

Acknowledgement

Integrating a Localized B_0 Shim Array into a Solenoid Transmit-Receive Coil for
Permanent Magnet Scanners

by

Celine Veys

A thesis submitted in partial satisfaction of the

requirements for the degree of

Master of Science

in

Electrical Engineering and Computer Science

in the

Graduate Division

of the
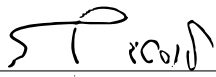
University of California, Berkeley

Committee in charge:

Professor Michael Lustig, Chair
Professor Ana Claudia Arias

Spring 2021

The thesis of Celine Veys, titled Integrating a Localized B_0 Shim Array into a Solenoid Transmit-Receive Coil for Permanent Magnet Scanners, is approved:

Chair Michael Lustig   Date 05/14/2021

Ana C. Arias   Date 05/14/2021

Date

University of California, Berkeley

Integrating a Localized B_0 Shim Array into a Solenoid Transmit-Receive Coil for
Permanent Magnet Scanners

Copyright 2021

by

Celine Veys

Abstract

Integrating a Localized B_0 Shim Array into a Solenoid Transmit-Receive Coil for
Permanent Magnet Scanners

by

Celine Veys

Master of Science in Electrical Engineering and Computer Science

University of California, Berkeley

Professor Michael Lustig, Chair

While low-to-mid field systems in MRI have nearly been abandoned for high-field, high-performance systems, recent improvements in MR hardware, algorithms, and computation have stimulated a resurgence in interest of upgrading lower-end magnets to achieve high performance at significantly lower cost, improved accessibility, portability, and siting. In this project, we upgrade a wrist 1T permanent-magnet system to reduce its field inhomogeneity while maintaining good SNR. We integrate a simple B_0 shim array into a solenoid TRX coil for reducing B_0 through localized targeted shimming. Through simulations and experiments, we demonstrate improved homogeneity with an initial 6-channel prototype, later upgrading to a full hardware-integrated 16-channel system, with negligible effects on the transmit field and received SNR.

Contents

List of Figures

Acknowledgments

Chapter 1

Introduction

1.1 Motivation

Magnetic resonance imaging, or MRI, has been integral in medical diagnoses in hospital settings. It offers low radiation and good image quality over other imaging methods, such as CT and PET scans. MRI can differentiate between different types of soft tissue. However, the superconducting magnets used in clinical scanners can be very expensive, each costing several millions of dollars. They are also large, immobile, have many siting requirements, and use a large amount of external hardware.

Permanent magnet scanners, by contrast, are a class of low-end, inexpensive magnets with the advantage of requiring no power and no cooling to maintain its field. These scanners tend to be small, shielded, safe and easy to site [14]. These have the advantage of imaging smaller subjects, like neonates and wrists. However, these systems can suffer from field inhomogeneity, drift and hysteresis, which decrease overall scan quality. Field inhomogeneity in particular can cause artifacts in images that could lead to misdiagnosis. Recent improvement in MR hardware, algorithms, and computation take advantage of the benefits of permanent magnet scanners while minimizing their disadvantages. One such hardware technique is called shimming, which improves the magnetic field inhomogeneity in these scanners. Localized non-linear shim arrays [6] are a possible solution [1]. Since they are placed close to the subject, shimming can be achieved with little current, thus making the system simple and affordable.

Figure 1.1 demonstrates the motivation for our work. A field map in a phantom of an Aspect Imaging Wrist II 1T system (Shoham, Israel) shows significant field inhomogeneities with global linear shims. We show that simulations and implementation of a 16 channel local shim array can provide substantial slice-by-slice local field homogeneity corrections in all directions. The aim of the study is to demonstrate the efficacy of using a localized shim coil array, wrapped around a solenoid RF coil both in simulations and practice. In addition,

we aim to demonstrate minimal interaction between our shim array and the RF system.
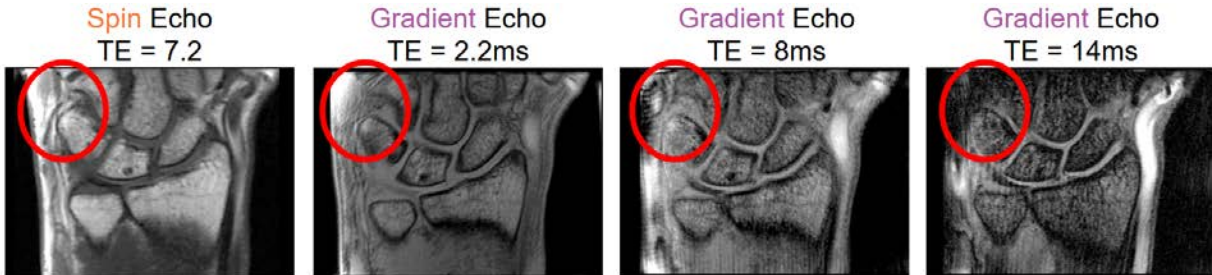
Figure 1.1: Comparison of gradient echo scans at increasing time-to-echo (TE) values against a spin echo scan. Spin echos are generally resistant to B_0 inhomogeneities, so we do not see significant artifacts. However, gradient echo scans, which perform faster image acquisitions than spin echos, are particularly susceptible to field inhomogeneities at higher echo times. All four scans were performed in the Aspect Wrist II 1T MRI System. As TE increases, we notice distortions in the magnitude in the form of ringing and signal loss as well as a drift in phase. The artifacts due to B_0 field inhomogeneity are especially noticeable in the upper left corner (circled in red). This disadvantage limits the different acquisition methods that can be implemented on a scanner with low field homogeneity such as echo planar imaging.

1.2 Related work

While there has been considerable work done in improving inhomogeneities in MRI scanners through various sequencing and reconstruction approaches, we examine several advancements in hardware technology in the field.

Higher order shims have been used to successfully homogenize the B_0 field. Spherical harmonic basis sets can be constructed and fit to a measured field distributions to erase B_0 variations. Our project uses the zeroth order global offset and three first order linear gradients. However, it has been shown that higher order harmonic functions contribute higher order symmetry and multiplicity, which can therefore model advanced target field shapes [5]. Imaging with nonlinear gradients allows for the projection of the sample onto curved isocontours, a technique that garnered attention to its ability to permit faster gradient switching. This has proven useful in application such as parallel imaging [6]. Higher order shims despite being ideal for low deviation 3D shims, need ample in-scanner space, and expensive current drivers.

Many shim designs utilize passive shimming techniques that strategically place ferromagnetic materials to counteract regions of inhomogeneity. This has been shown to successfully

generate low-order homogeneous magnetic field harmonics while minimizing the amount of ferromagnetic material used [11]. Despite the limitations of placement and immutability of passive shims, there have been examples of simple diamagnetic passive shims that significantly reduce static field inhomogeneity in brain imaging [19]. This technique was improved upon through construction of sample-specific passive shims comprised of both diamagnetic and paramagnetic materials that were shown to significantly homogenize a mouse brain at 9.4T [12]. Passive shimming procedures usually suffer from flexibility in managing spherical harmonic field expansion or inability to produce optimal overall field homogeneity, so algorithms have been developed to combine the strengths of the magnetic-field-based and harmonic-based shimming methods. [13]

Active shimming is a more flexible alternative to passive shimming in that it is constructed of mutable current-carrying filaments. These shims use current-induced magnetic fields, calculated by Biot-Savart law (Equation 2.1) to fix inhomogeneities in the scanner's magnetic field. The flexibility of active shims allows for several innovations. For example, a shim coil can be shaped and placed in irregular patterns, unlike passive shims, and their use of non-magnetic conductors such as copper does not restrict the placement of these coils to static positions around the subject [18]. It also allows for the combination RF and DC coils into one element to reduce space and power [7, 16, 1]. Using these nonlinear localized shim coils allows for a space-conserving, low-power field inhomogeneity solution, and we aim to implement them in this project.

1.3 Project Parts

1.4 Contribution

Chapter 2

Background

2.1 Permanent Magnet Scanners

Permanent magnets are susceptible to large inhomogeneities due to the nature of their construction, so they must be carefully designed to be within acceptable homogeneity ranges to acquire high quality images. This is nontrivial due to fabrication errors and thermal contraction within the permanent magnets.

A Halbach magnet array is an arrangement of permanent magnet scanners such that the magnetic field they generate is homogeneous (i.e. having constant and unidirectional magnitude) and radially-oriented for an infinitely long scanner [2]. This is effective for scanning small subjects, as it maintains sufficient field homogeneity for MRI acquisition. This arrangement is also safer because the field strength outside the scanner is negligible.

The experiments in this project are performed using an Aspect Wrist II 1T MRI System, which implements a Halbach magnet configuration to generate its magnetic field.

2.2 Magnetic Shimming

In order to get quality images, without artifacts, the magnetic field deviation in a MRI scanner should be on the order of 1 parts per million for low-field scanners. High-field superconducting scanners and especially permanent magnet scanners suffer greatly from field inhomogeneity, so a technique called shimming, where external magnetic fields are added to the scanner, is employed to remedy such deviations.

Shimming is performed by taking a measurement of the magnetic field within the scanner and generating a magnetic field to oppose any deviations, then adding this opposing magnetic field to the original field.

There are two main categories of shimming: passive and active. Passing shimming utilizes ferromagnetic material placed in or around the scanner to adjust the magnetic field inside the scanner. While it does not require external power and has relatively low system complexity, passive shimming is less mutable than active shimming, since it is relatively difficult to alter the shape and position of preset magnets.

Active shimming, on the other hand, uses non-magnetic conductors that have the potential to carry variable current, adjusting for magnetic field deviation over time. These resistive coils generate magnetic fields using low power, according to Biot-Savart law (Equation 2.1), and are relatively easy to construct. It also allows for dynamic shimming, the process of shimming 2D slices successively within a volume. However, it requires external power and often a setup that relays variable power to the shim array.

2.3 Biot-Savart Law

In order to use active coils as shims, we must examine the magnetic field contribution of each coil. This is determined by Biot-Savart law (Equation 2.1) that describes the magnetic field produced by a constant current in a conductor, given the length of the wire and the point at which we are measuring the magnetic field.

$$\vec{B} = \frac{\mu_0 I}{4\pi} \int \frac{\partial \vec{\ell} \times \hat{r}}{\|\vec{r}\|^2} \tag{2.1}$$

where μ_0 is the magnetic vacuum permeability, I is the current driven through a wire, $\partial \vec{\ell}$ is the length vector of the current carrying conductor, and $\hat{r}$ is the unit vector for $\vec{r}$ [8].

2.4 Calibration and Sequencing

In order to acquire images through the scanner, we initially used the Aspect Neonate scanning software to run calibrations and our pulse sequences. A pulse sequence is comprised of radiofrequency (RF) pulses, gradient pulses, and signal acquisition that stimulate and measure the precession of protons in a subject. These sequences are vital to MRI. Gradient echos and spin echos are two classes of pulse sequences (Figure 1.1). Most other pulse sequences are variants that implement the fundamental principles of these two classes. The calibrations done before running the sequence are to set appropriate values for the center frequency, coil tuning, global linear shim values, and RF values.

While a graphical user interface was useful in setting up our scans for shimming, we later developed a codebase in MATLAB that allowed us to automatically complete the shimming process.

Chapter 3

Methods

3.1 Local Shim Array and RF Solenoid

All studies and experiments throughout this research project used a wrist RF solenoid transmit-receive coil placed inside a plastic scanner sleeve. The RF solenoid creates a B_1 field in the x-direction, while the B_0 field, the main field created by the permanent magnets in the scanner, is in the z direction (Figure 3.1).

This allows us to construct a shim array decoupled from the B_1 field and maximally contributing to the B_0 field. The solenoid can be approximated as a rectangular prism of dimension 10cm x 10cm x 5cm, with its sagittal faces removed such that a hand and wrist can be inserted. The coronal faces are the larger 10cm x 10cm sides are the solenoid, while the axial faces are the smaller 10cm x 5cm sides. The surface area usable for the shim array is 300 cm^2. The strength of the magnetic field generated by a current-carrying wire at a point is inversely proportional to the square of the distance from the wire to that point (Equation 2.1). The closer the shim array is placed to the solenoid, the less current, and consequently power, is needed to achieve a quality shim. We use these facts to simulate and construct our shim array coils flush onto the solenoid so that they save power and space. The placement of the local shim array on the solenoid is depicted in Figure 3.2.

3.2 Simulations

As described in Magnetic Shimming, Biot-Savart can be used to calculate the B_0 field contributions within the field of view (FOV) of the RF solenoid from the shim coils we simulate. We used a toolbox in MATLAB [15] to simulate coils with 1A of current. This is shown at the top of Figure 3.3.

Our first simulation was with six circular coils, evenly spaced across one face of the
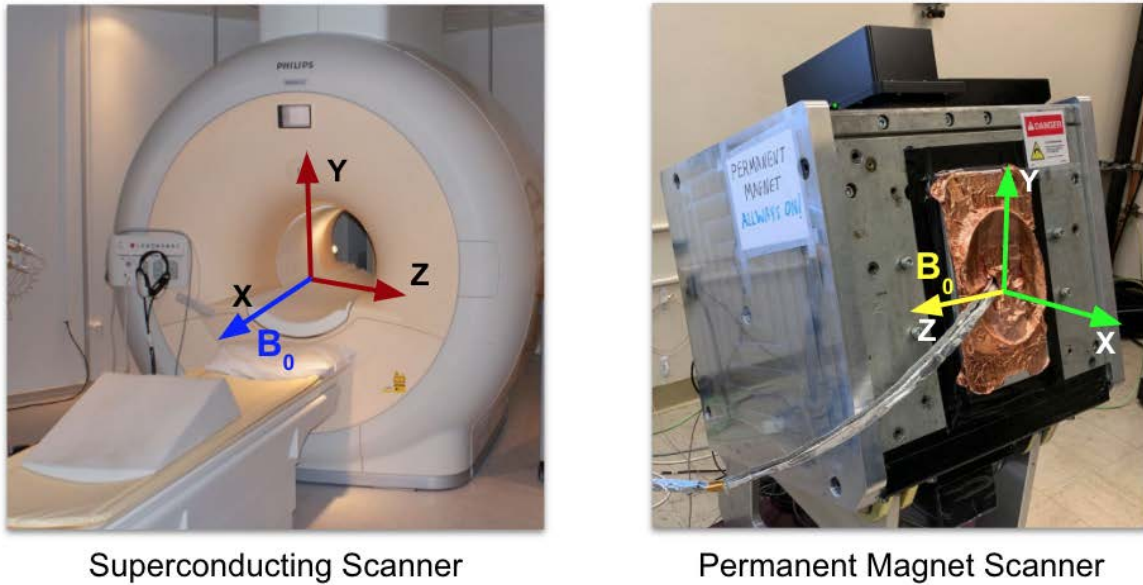
Figure 3.1: The magnetic field directions for a superconducting vs. a permanent magnet scanner. The B_0 field in a superconducting scanner is parallel with the length of the bore, in the x direction, along the body of the subject. In a permanent magnet scanner, however, the B_0 field is in the z direction, perpendicular to the subject. This allows the RF coil to be a solenoid, so the B_1 field's direction is out of the bore in the x direction. This is perpendicular to the B_0 field, thus making it easy to place our shims flush onto the solenoid without coupling to the B_1 field.

solenoid. We created a 3x2 array, each coil with a radius of 2.5 cm, whose centers were 2 cm apart. This way, they all fit uniformly on one of the rectangular surfaces of the RF solenoid (Figure 3.4). A bottle phantom doped with copper sulfate ($CuSO_4$) (Figure 3.4) is placed inside the solenoid. We acquired fieldmap data through a two-scan gradient echo sequence with a delay in acquisition.

3.3 Regularized, Constrained Least Squares Optimization

We employ targeted shimming – that is, we find optimal x values for each slice in a particular direction of a scan. The magnetic field contribution of each coil is represented as a column in a matrix A, and the target measured magnetic field (i.e. a fieldmap) is represented by $-b$, with each component of x representing the scaling for each coil. A
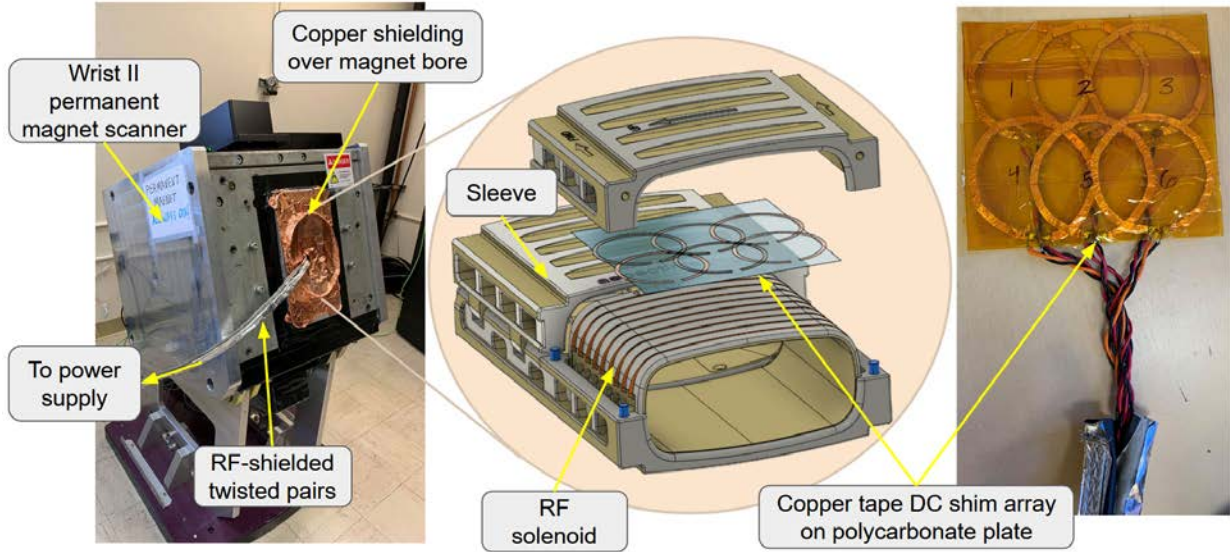
Figure 3.2: This is the setup for our experiment. The shim loop array is placed between the RF solenoid and the sleeve cover. The bore is copper shielded as a temporary RF interference mitigating solution that does not require scanner modification. The rightmost picture is the constructed shim loop array connected to shielded twisted-pairs that are also RF shielded.

least-square minimization is performed over each targeted slice i:

$$\min_{x} \quad \|A_i x + b_i\|_2 + \lambda\|x\|_1 + \psi\|(A_{i-1} + A_{i+1})x + (b_{i-1} + b_{i+1})\|_2$$
$$\text{subject to} \quad |x| \le 2, \tag{3.1}$$

where we add $i-1$ and $i+1$ terms to ensure that the fieldmap gradient is smooth through the slice. We scale this value by ψ, which is selected by how much adjacent slices should be weighted in comparison to the main slice. To reduce the total amount current used in the system, we also include an ℓ-1 regularization, scaled by λ, and employ a hard constraint on the current so that the coils do not overheat.

The bottom of Figure 3.3 is an example of the results of this optimization.
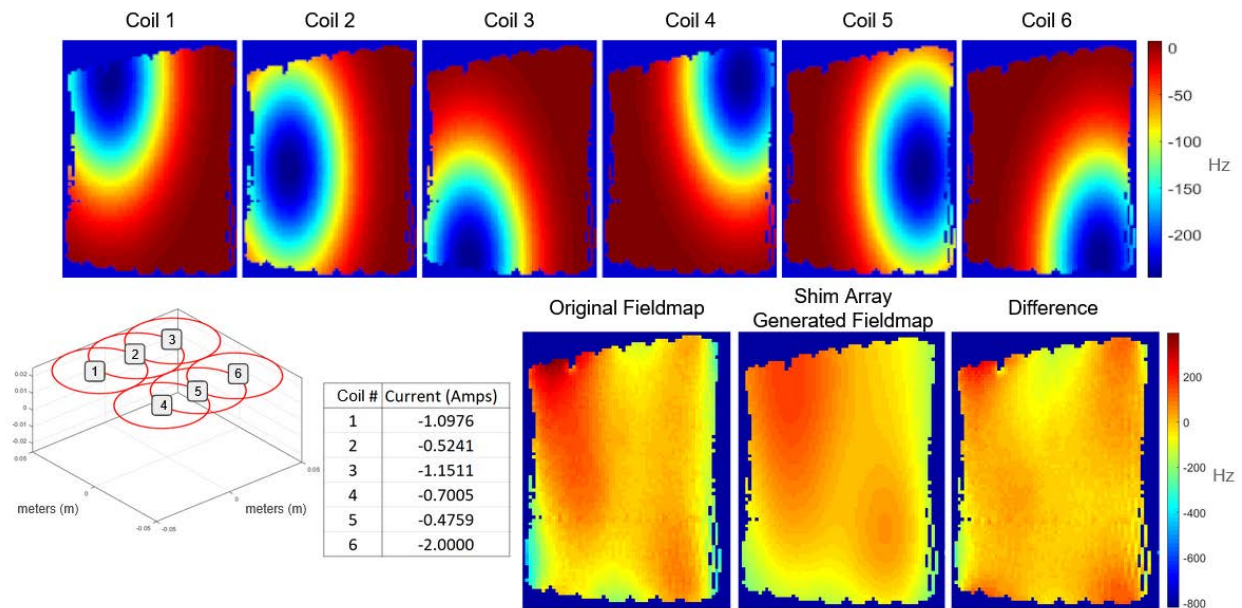
Figure 3.3: The simulations for the initial prototype of our shim array and the least-squares shim solution. The top row depicts the fieldmaps of the coils constructed in simulation. The bottom left picture shows the coil placement on the solenoid. The three bottom right pictures depict the original fieldmap, without any current applied, the fieldmap generated in simulation from the output of Equation 3.1, and the difference in those fieldmaps (i.e. the resultant shim). The table in the middle shows the optimal current values for each coil, as determined by the the solution of Equation 3.1.
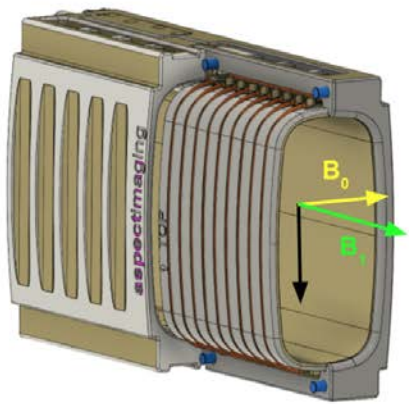
Magnetic field orientations on sleeve Shim array placed onto RF solenoid
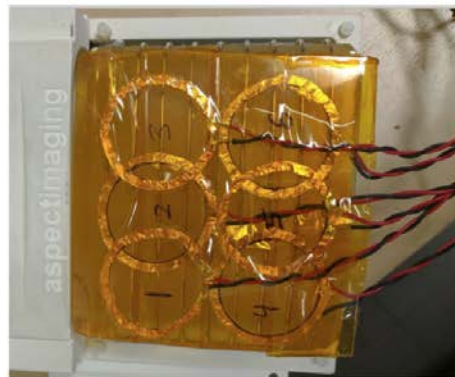
Figure 3.4: Shim array placement and bottle phantom. The far left is the RF solenoid and its sleeve (cover removed). The B_0 field direction is to the right, while the B_1 field direction is out of the bore. The placement of the shim array on top of the RF solenoid is shown in the middle. On the right is a copper sulfate doped bottle phantom, inserted into the solenoid shown on the far left.

Chapter 4

Experimental Design

4.1   Shim Array Design

As established previously, the optimal placement of the local shim array is directly on the solenoid, to conserve both space and power. However, there were a couple constraints we still had to consider when placing our coils:

- **Scanner Space**: The most apparent obstacle was tightness of the scanner bore and the consequently compact sleeve. The available space between the solenoid and its sleeve cover is less than half a centimeter, so the coils, the wires that are soldered to them, and the surface on which the coils are mounted, must all be comfortably within these limits to avoid damage to the shim array.

- **Coupling**: One of the most difficult constraints to control for before construction is coupling with the RF solenoid. With little space to separate the solenoid and the shim array, as well as many wires that were routed out of the scanner, the likelihood of capacitive coupling and RF interference was high.

Initial Prototype

As a proof of concept, our initial prototype was a 3x2 array of circular coils (Figure 3.4), constructed with copper tape, a thin, non-magnetic material with very low resistance (less than 1Ω). Since the copper tape was fragile, constructing non-circular shapes was difficult, so all our copper-tape coils were circular. To reinforce their durability, our 2mm wide coils were taped onto a 0.5mm flexible polycarbonate plate, which was later sandwiched between the RF solenoid and its sleeve cover. Each coil was evenly spaced with a radius of about 2.5cm to maximize coverage of the field of view. We placed the polycarbonate plate parallel to the largest face of the solenoid, such that the magnetic field that its coils would generate would be in the same direction as the B_0 field. While the magnetic field generated by these coils

matched simulation, the width of the copper tape led to some coupling with the solenoid. In addition, when another 3x2 array was placed on the opposing face of the solenoid, the new 12-coil system exceeded its allocated space on the sleeve.

Second Iteration

In order to improve upon our prototype, we opted to use 32-gauge magnet wire as a thinner, more flexible replacement to copper tape. While they were not adhesive themselves, placing them on Kapton tape mimicked the design of our prototype. This made fitting the shim array onto the sleeve more straightforward. After verifying this setup worked well for the main B_0 field direction, we added four more coils to the array, two on each of the remaining faces of the solenoid, so that the magnetic field could be shimmed in other directions. This shim array is shown in Figure 4.1. Despite minimizing the coupling on the main faces of the solenoid, the new shim array coupled with the tuning capacitors on the axial sides of the solenoid. This issue was remedied by increasing the spacing between the capacitors and the shim array.

Figure 4.1: The second iteration of our shim array, made with 32-gauge magnet wire. This is wrapped around the RF solenoid when scanning.

4.2   Current Driver Circuit Board System

When we developed our initial 6-channel prototype, we used five single-channel and three two-channel power supplies to drive currents into our coils. These multiple power supplies not only required tedious, slow manual adjustments for every shim, but they also contributed a significant amount of noise that affected the SNR of our scans.

Thankfully, a team at Massachusetts General Hospital gifted us a current driver system [3] consisting of three printed circuit boards (PCBs): a Teensy microcontroller board, fiber optic relay board, and the DC current driving amplifier board. This system not only significantly organized our setup and reduced issues with noise, current switching, and shimming speed, but it also made dynamic shimming a viable next step for this project.
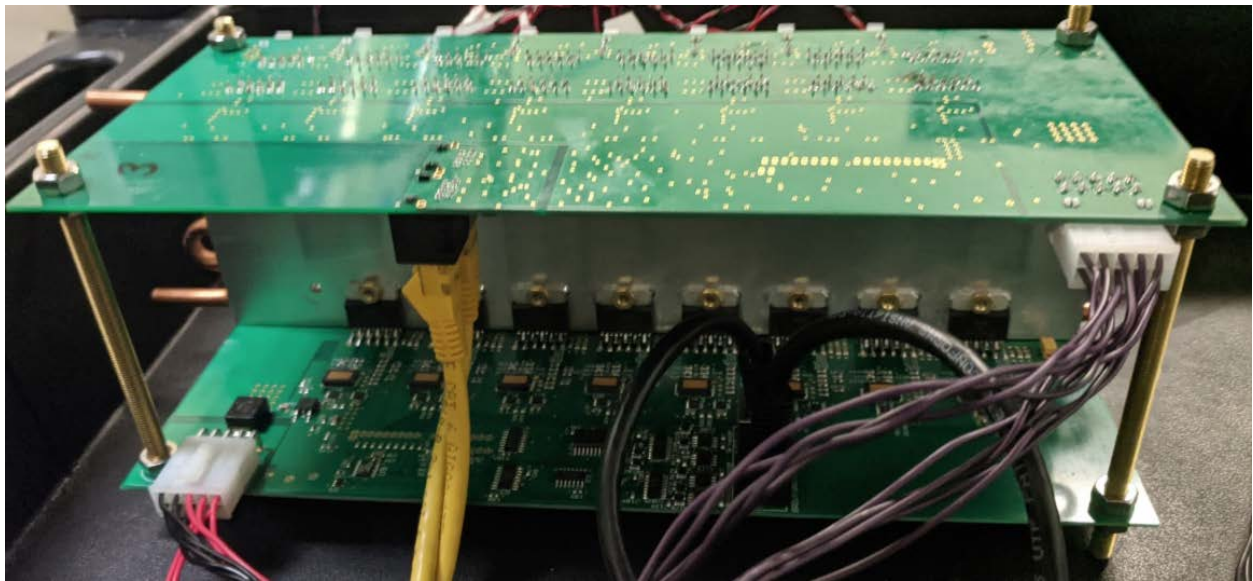
Figure 4.2: The fully connected current amplifier system. The two amplifiers boards are connected to a heat sink to dissipate heat from the OPA549 amplifiers and supported with brass rods. Each amplifer board is connected to the power supply via molex connectors and to the fiber optic board via CAT-6 cables.

Teensy Microcontroller Board

The Teensy microcontroller can be programmed to calibrate and read/write commands for each current channel. The board that the Teensy is soldered to (Figure 4.3) also has fiber optic connectors such that it can send data quickly without loss over several meters. An 8-channel 16-bit DAC on the amplifier board is used to update the current values for each channel.
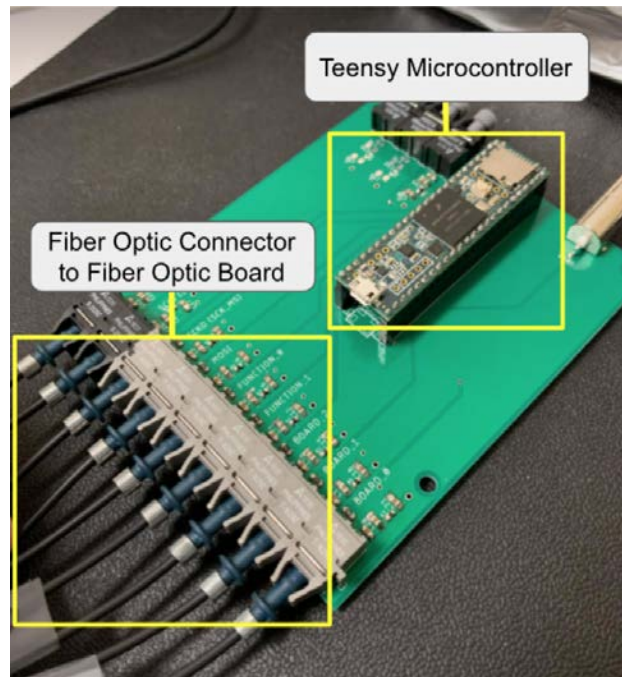
Figure 4.3: The Teensy board, which supports the Teensy microcontroller that can be programmed from a computer via USB cable. Data is then sent to the fiber optic board via fiber optic connectors and cables.

Fiber Optic Board

This board (Figure 4.4) acts as a relay between the microcontroller and current amplifier boards. It can take up to 8 amplifier boards, though we only use two for our system, since each amplifier board has 8 channels, and we use 16 channels total. For our application, since the operator and scanner room are the same, we do not need the fiber optic board, as the fiber optic cables are intended to be passed through an RF shield between the console and the scanner room. However, there is virtually no delay in sending information between the boards because of the fiber optic cables. This board is connected to the amplifier boards using RJ45 CAT-6 cables.

Current driver boards

This is a low-cost (about \$75 per channel), feedback controlled DC amplifier system (Figure 4.5) designed for shim array such as ours. They are robust against noise and have very high slew rate in order to ensure rapid switching. The amplifier boards each use 16 OPA549s linear power stage op amps in a push-pull configuration to drive all 8 channels available on each board. While each channel is capable of supplying 8A DC, we only use at
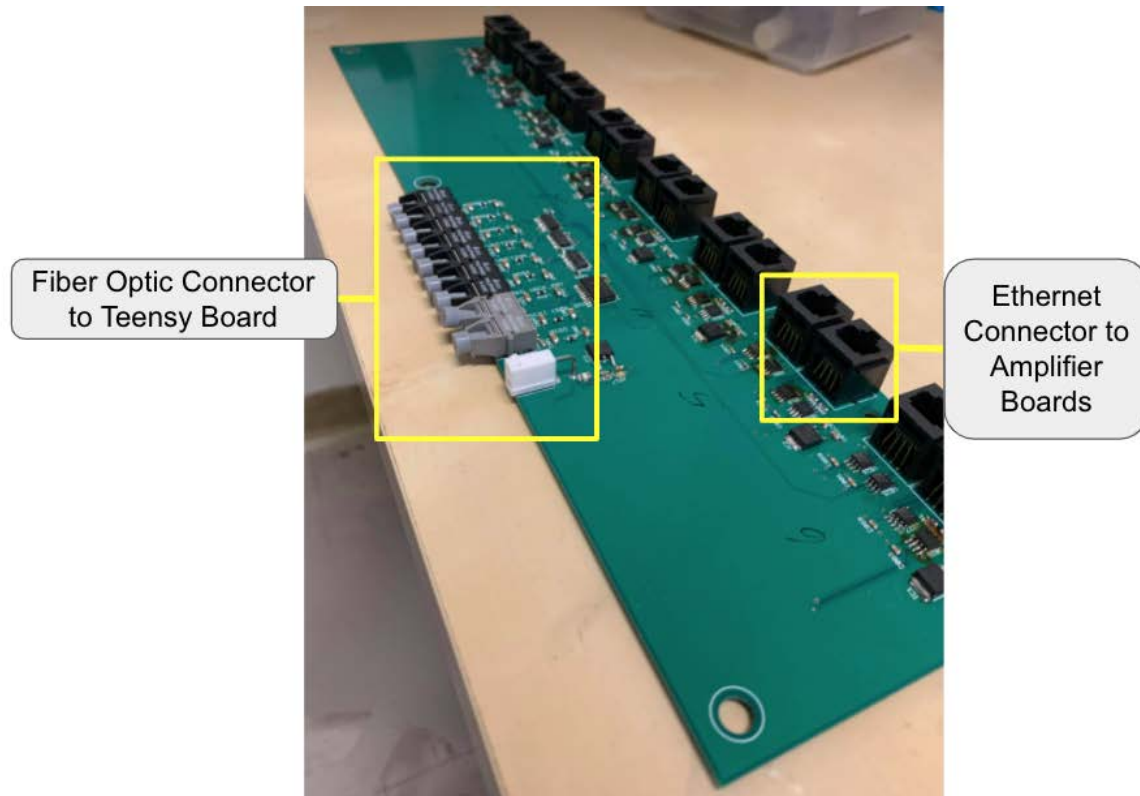
Figure 4.4: The fiber optic board, which has fiber optic connectors that receive the cables from the Teensy board. It also has eight CAT-6 cable connector ports, each of which can connect to one amplifier board. Thus, one fiber optic board is capable of supporting a system of 64 amplifier boards.

most 2A (5W per channel) to prevent overheating as discussed earlier. Each channel uses a feedback control topology to ensure stability of the current output, with more than 45 degree phase margin and around 50 μs rise time. The feedback loop compensation elements is set up to compensate a 10 μH reactive load [3]. Though our application is relatively low-current, heat sinking the op amps is still necessary for the system to work as expected.

4.3   Shim Process Automation

The circuit board system greatly contributed to our ability to automate our shimming process. This process is consisted of four main steps:

1. **Characterization** - We measure the magnetic field of each coil and the linear gradients
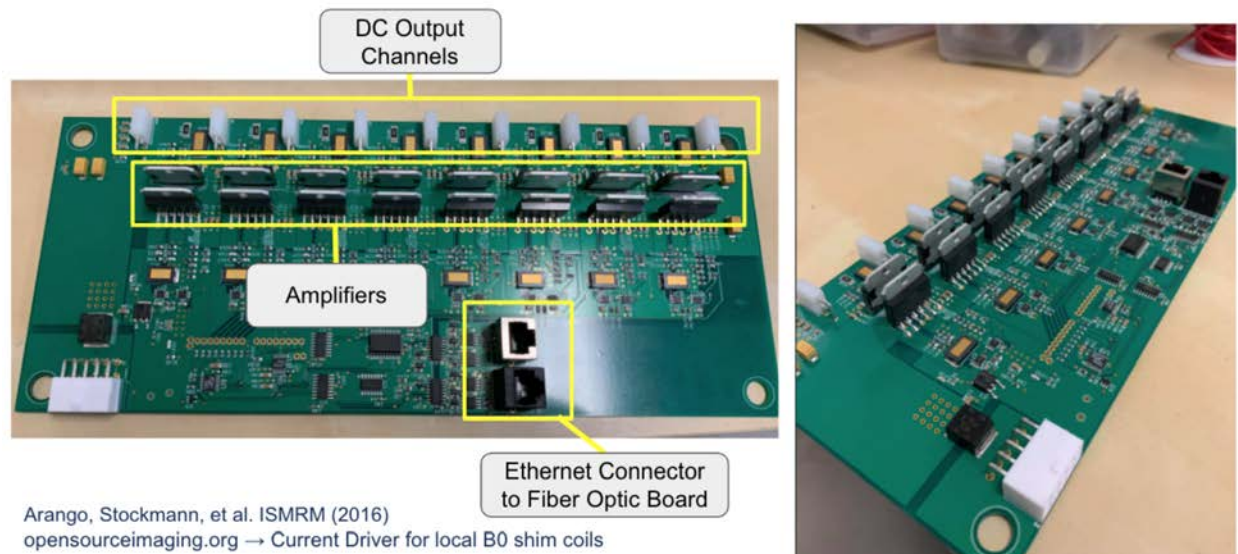
Figure 4.5: Two amplifier boards. Each amplifier board has 8 DC output channels (one extra channel is included for debugging) and 16 amplifiers, two for each channel. It includes current sense resistors to ensure feedback and stability in the circuit and has several probe points to aid in debugging, as well as a DAC that the Teensy programs. Its shielded CAT-6 cable connectors allows it to be connected to the fiber optic board.

for a given current (in our case, 1A for each coil and 0.05 amplitude change for the linear gradients) to construct the least squares matrices described in Equation 3.1 (Figure 5.2). We first calculate a fieldmap with no induced magnetic field as a reference, followed by the fieldmaps of all 19 components of our minimization problem (16 coils + 3 gradients). This step can be pre-computed once and reused for future shims, as long as the shim array and phantom do not change or move.

2. **Least Squares Minimization** - Each of the measured fieldmaps are masked and reshaped into vectors and concatenated into a single matrix. We then solve Equation 3.1 for the target slice.

3. **Teensy Programming** - The current solution is then uploaded for each coil onto the Teensy microcontroller.

4. **Slice-Selective Frequency Calibration** - To account for measurement errors regarding the center frequency from the **Characterization** step, we run the slice-selective frequency calibration sequence, which re-centers the frequency after potential drift.

Before receiving the boards, our characterization and Teensy programming steps required manual adjustments of several power supplies. Despite better automation, we still had to

manually write Teensy commands into its software for both characterization and shimming. We also manually updated the linear gradient values after taking characterization scans.

Therefore, we designed a fully automated shimming process in MATLAB, in which we built an interface with the Teensy, ran all the necessary pulse sequences, and sent SQL commands to the database where the linear gradient and center frequency information is stored. What previously took about 5-6 hours to operate manually was now a process completed in less than half an hour.

Chapter 5

Experimental Results

5.1   Verification

The fieldmaps of the coils in the scanner were measured and compared with our simulations (Figure 3.3) to verify similarity. Satisfied with the results, we verified that the SNR did not drop significantly between a scan without and with the shim array, indicating minimal coupling between our shim array and the RF solenoid (Figure 5.1). After upgrading our shim array from 6 to 16 channels, the fieldmaps of each coil driven with 1A independently (Figure 5.2) were again measured, yielding similar results to simulations. As mentioned previously, permanent magnets suffer from temperature drift, so the center frequencies in these fieldmaps are not persistent over time. Despite attempts to correct this drift using frequency calibration, their differences are still apparent between each plot. In addition, all simulated coil fieldmaps reflect the noise of all 16 coils, which later show up in our shimming simulations.

5.2   Results

Each of Figures 5.3, 5.4, and 5.5 depict targeted shimming for the slices 18, 20, and 21 (3cm, 6cm, and 7.5cm from the center of the slice respectively). On the top row, plotted in Hz, from left to right are: the original fieldmap without currents applied to the coils, the fieldmap we expect to get after shimming in simulation, and the shimmed fieldmap we get in experimentation. On the bottom, the middle plot is an overlayed histogram of the original fieldmap, simulated fieldmap, and shimmed fieldmap frequency distributions. In all cases, the simulated and experimental shims are very similar to one another and both have a significantly narrower distribution than the original fieldmap. The bottom-left and bottom-right plots are vertical and horizontal cross sections respectively. Again, we see that the simulated and shimmed results are very similar, with frequency offsets close to zero. There is a significant improvement from the inhomogeneity in the original fieldmap. We calculate
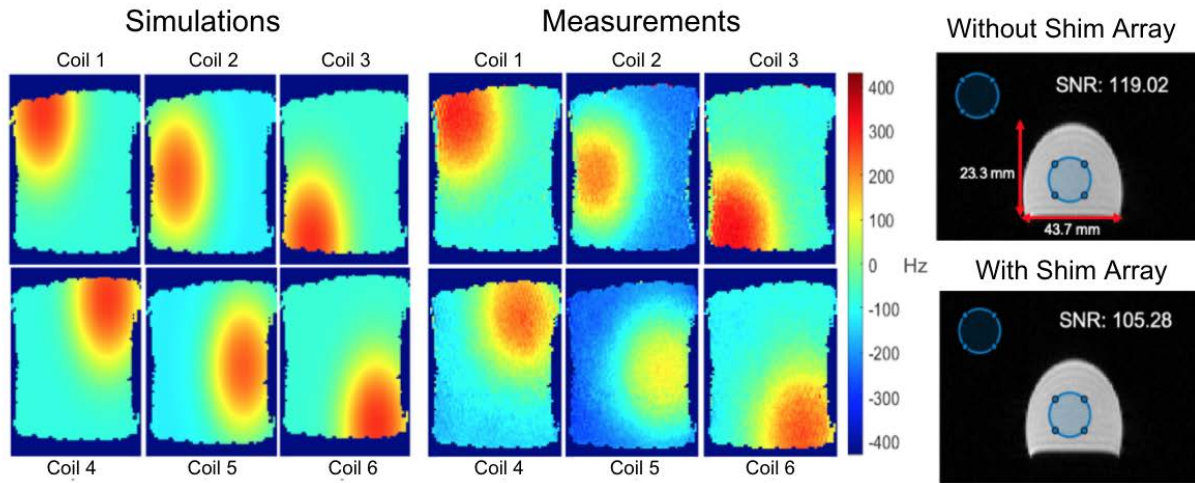
Figure 5.1: Simualations vs. measurements of the shim array and an SNR verification. A comparison of the simulations from Figure 3.3 and the magnetic fields in the B_0 direction generated by the coils in Figure 3.2 is shown on the left. On the right is the SNR that is determined by calculating the ratio between the standard deviation inside and outside the field of view. With only an 11% decrease between the fieldmap without the shim array and with it, we determine this be satisfactory.

the deviation in ppm for each of the instances through the equation:

$$\text{ppm} = \frac{\text{std in Hz} \cdot 10^6}{42.58\text{MHz}}$$

For these three instances, we find that the overall inhomogeneity measured in the magnetic field after applying the minimization solution to our local shim array is close to the 1 ppm field variation at 1T reportedly required for some MRI sequences [17].
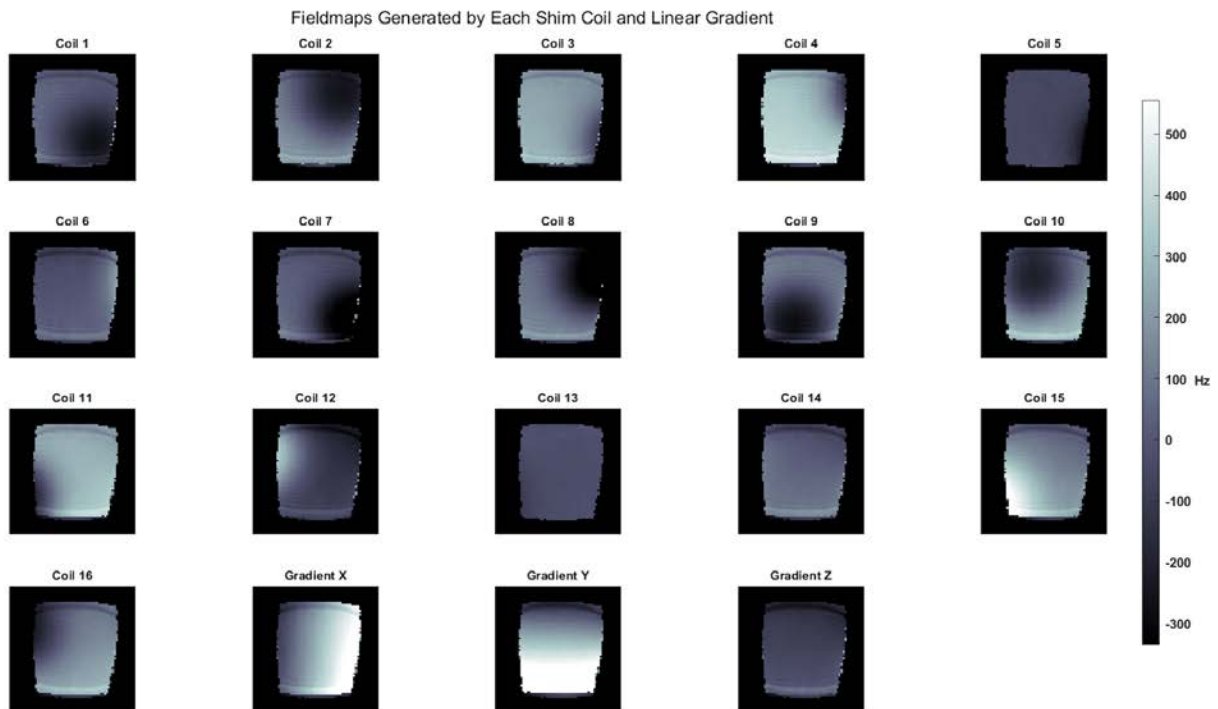
Figure 5.2: Coil fieldmaps from experiment. Each picture in this figure represents a fieldmap at slice 16/32 (middle of scanning volume) generated with a gradient echo sequence after each coil was driven with a current of 1A independently. The last three fieldmaps are generated by the linear shims, each independently with a change in amplitude of 0.05 in the coronal direction. The field strength is measured in Hz.
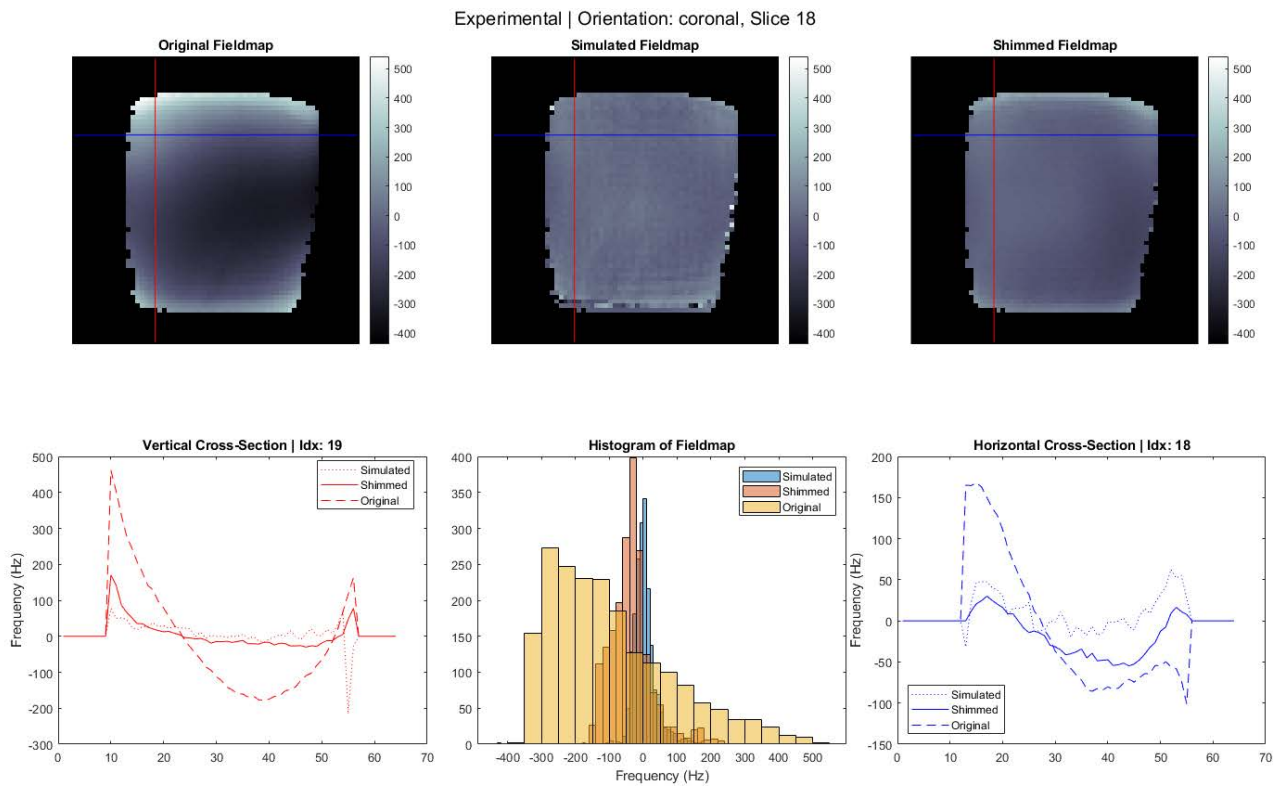
Figure 5.3: Experimental results for slice 18 (+3cm from center) in the coronal orientation. The overall deviation without the shim array was calculated to be 3.1179 ppm. The overall deviation was calculated to be 1.0663 ppm.
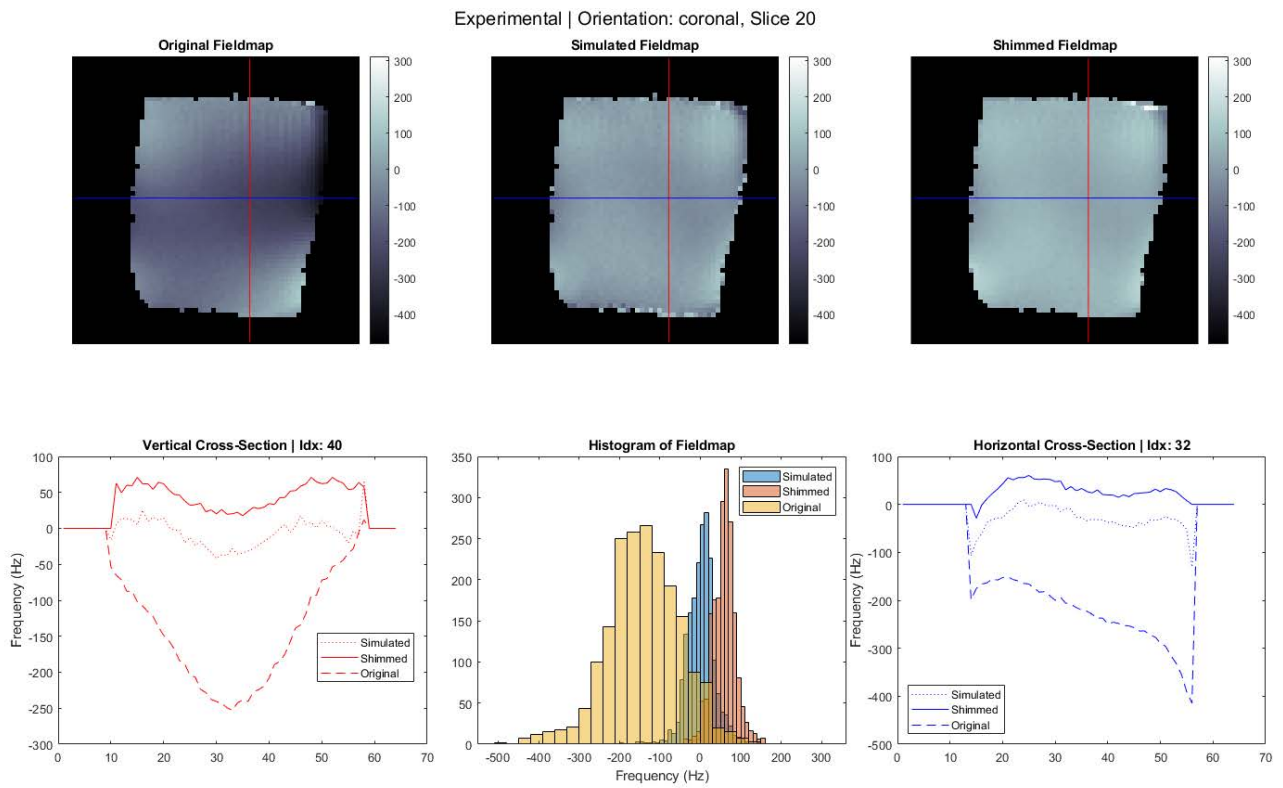
Figure 5.4: Experimental results for slice 20 (+6cm from center) in the coronal orientation. The overall deviation without the shim array was calculated to be 2.1243 ppm. The overall deviation with the shim array was calculated to be 0.7727 ppm
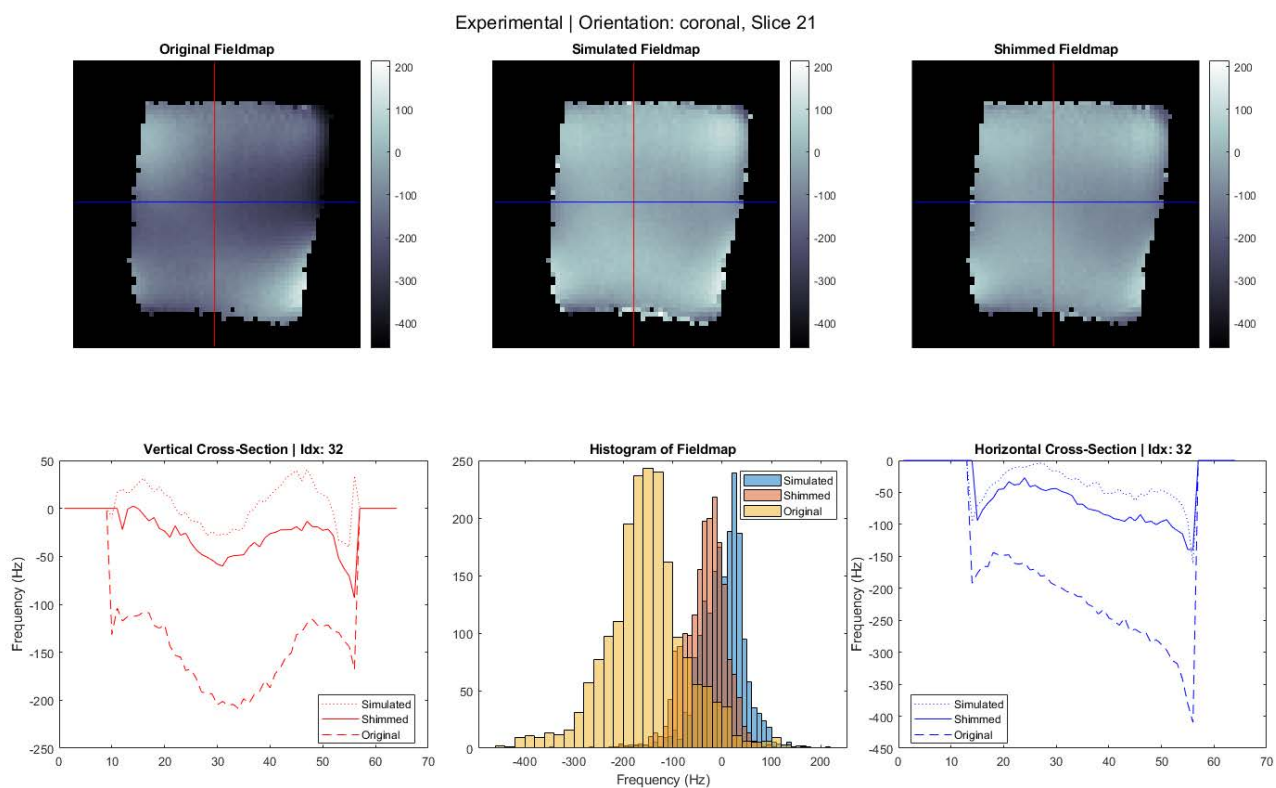
Figure 5.5: Experimental results for slice 21 (+7.5cm from center) in the coronal orientation. The overall deviation without the shim array was calculated to be 1.9430 ppm. The overall deviation was calculated to be 0.9981 ppm.

Chapter 6

Shim Coil Selection Algorithms

For the majority of our project, we have used uniformly spaced, identically-sized circular shims because they are easy to simulate and construct. However, this is not necessarily the best configuration to perform targeted or dynamic shimming. In order to find a more optimal configuration, we developed a few algorithms that used different methods to search a set of possible shim placements and sizes and maximize their shimming efficacy for our particular scanner. We use the same search space for each algorithm: 138 coils, ranging from 2cm to 5cm in radius, whose centers are placed on an evenly spaced grid.

6.1   Mixed Integer Optimization

Since coil selection schemes require sparse solutions, utilizing an ℓ-1 regularization may be an intuitive first step. However, integer programming also proves to be a useful tool in solving these sparsity problems.

Integer Programming

In order to understand the first algorithm we implemented, we first examine a class of optimization programs called integer programs. Often, optimization problems can be formulated in with continuous real objectives and constraints. This is the case for the objective we defined earlier in the optimization problem 3.1. However, sometimes it is necessary to impose integer constraints on problems whose solutions cannot be continuous, such as how many coils should be used in an experiment. A pure integer program is one in which all decision variables must be integers, whereas a mixed integer program can have some, but not all, variables restricted to be an integer.

Unfortunately, integer constraints make our problem non-convex, and therefore significantly more difficult to solve. In fact, they are theoretically intractable. CVX employs the use of combinatorial/probabilistic optimization as well as a combination of a continuous

optimization algorithm, such as an interior-point method, and an exhaustive search, such as a branch-and-bound to solve such problems. However, it is not guaranteed that the solver will find a global solution in a reasonable amount of time [4]. Nevertheless, we chose to use mixed integer optimization to search over a pre-constructed space of shim coils to show we could find a better solution (i.e. an arrangement of shim coils that would eventually produce a better shim) than our initial uniform-coil prototype.

Mixed Integer Optimization Algorithm

This algorithm consisted of minimizing a least squares objective function (Equation 3.1) with binary constraints such that it reduces the search space to the appropriate size. Since this is computationally expensive as described in the previous section, it is implausible to start with a search space that is too large, so we empirically selected a reduced search space that would allow for reasonable convergence time. This space consisted of 138 coils, ranging from 2cm to 5cm in radius, and whose positions were determined by a finely spaced grid on the surface area of the sleeve.

This, however, was still too large, so we tested the convergence times for search spaces of cardinality close to our coil-number goal of 16. We chose 36 hours to be the maximum reasonable time to wait for the program to converge, and determined that the cardinality could not be more than 32 coils. Therefore, in order to reduce our space from 138 to 32, we implemented another algorithm, this one convex and iterative, to perform least squares as we do when regularly shimming and sorting the 2-norm of the current solutions of these problems in descending order. This way, we determine the "most important" coils in each iteration, and use them in the subsequent one until we reach 32 coils. Then, we employ the mixed integer program to more robustly search from an optimal selection of 16 coils.

The formula we use for this algorithm is the following:

$$
\begin{aligned}
\min_{x} \quad & \sum_{i=1}^{N} \left(\|A_i x + b_i\|_2 + \psi \|(A_{i-1} + A_{i+1})x + (b_{i-1} + b_{i+1})\|_2 \right) + \lambda \|x\|_1 \\
\text{subject to} \quad & |x| \leq 2 * p, \\
& \sum p = 16
\end{aligned}
\tag{6.1}
$$

where p is a binary vector which constrains the total number of coils used in the solution x to be 16, i are the slice indices, N is the total number of slices, and the A matrix and b vector are defined as they are in Equation 3.1. Note that the binary vector does not include the linear gradients, because they are always meant to be selected, but they are included in the objective function.

Algorithm 1: Iterative sort reduction and mixed integer optimization

---

input: A - $O \times C \times N$ matrix of fieldmap contributions from C coils and gradients with O observation points for N slices

b - $O \times N$ vector containing O observations for N slices of the target fieldmap

output: The 16 coils with the most significant current contribution, i.e. the final results of selectedCoils.

selectedCoils = [1:138]

currentNumCoils = 138

reduceCoilNumBy = 5

while currentNumCoils>32 **do**

    Use CVX [9, 10] to solve the problem 3.1

    Sort norm of solution x from greatest to least, and select top

      currentNumCoils-reduceCoilNumBy

    currentNumCoils-=reduceCoilNumBy

end

Use CVX [9, 10] to solve the problem 6.1

selectedCoils = selectedCoils(p==1)

6.2 Joint Sparsity Optimization

Another algorithm, joint sparsity optimization, used the problem in Equation 3.1 but added a regularization term as follows:

$$\min_{x} \quad \sum_{i=1}^{N} \|A_i x_i + b_i\|_2 + \psi \|(A_{i-1} + A_{i+1})x_i + (b_{i-1} + b_{i+1})\|_2 + \lambda \sum_{i=1}^{N} \|x_i\|_1 \tag{6.2}$$

$$\text{s.t.} \quad |x| < 2$$

Here, we sum over the all slices and their corresponding x values in order to implement the "joint" part of joint sparsity. N is the total number of slices, and the other hyperparameters are again defined as they are in Equation 3.1. The ℓ_1 regularization on the coil current forces many of the current values to zero, which allows the most significantly contributing coils to get the most current. The goal of this algorithm is to identify the 16 most useful coils, which is achieved by iterating over possible values of λ. The value of λ is inversely proportional to the number of significant coils, so the higher it is, the fewer coils are output.

Algorithm 2: Joint Sparsity Optimization

---

input: A - $O \times C \times N$ matrix of fieldmap contributions from C coils and gradients
with O observation points for N slices
b - $O \times N$ vector containing O observations for N slices of the target
fieldmap

output: The 16 coils with the most significant current contribution

$\lambda = 1$

while numSigCoils != 16 **do**

    Use CVX [9, 10] to solve the problem 6.2

    numSigCoils = count(coils with significant current contribution)

    if numSigCoils > 16 **then**

       | increase λ

    else if numSigCoils < 16 **then**

       | decrease λ

    else

       | break

end

6.3   Matching Pursuit Optimization

Matching pursuit (MP) is a greedy algorithm that selects basis functions to fit to a signal. We assign each of our coil fieldmaps as our basis functions, and the original scanner field map as the signal to which we want to fit. This algorithm initializes a residual to be the target function, or in our case, the difference between the target function and the best fit gradient shim, since our optimization functions always include the linear gradient shims. From there, we iterate to find the coil that fits to the residual and add that to the solution. Then, we calculate a new residual as the difference between the target function and our solution's best fit. This iteration continues until we have 16 coils.

Algorithm 3: Matching pursuit

---

input: $\boldsymbol{A}$ - $O \cdot N \times C$ matrix of fieldmap contributions from C coils and gradients
with O observation points for N slices

$\boldsymbol{b}$ - $O \cdot N$ vector containing O observations for N slices of the target fieldmap

output: The 16 coils with the most significant current contribution

selected = [gradientX, gradientY, gradientZ]

selectedFieldmaps = A(:, selected)

optVals = solution to Equation 3.1 for selectedFieldmaps

residual = b - selectedFieldmaps*optVals

for *i = 1 to 16* **do**

> nextSelected = argmax(A · residual)
>
> append nextSelected to selected
>
> selectedFieldmaps = A(:, selected)
>
> optVals = solution to Equation 3.1 for selectedFieldmaps
>
> residual = b - selectedFieldmaps*optVals

end

6.4   Algorithm Comparisons

Figures 6.1 and 6.2 depict the differences in coil placement and configuration for each of the algorithms as well as the difference in mean-square error (MSE) of the best shim each algorithm could achieve per slice in two directions.
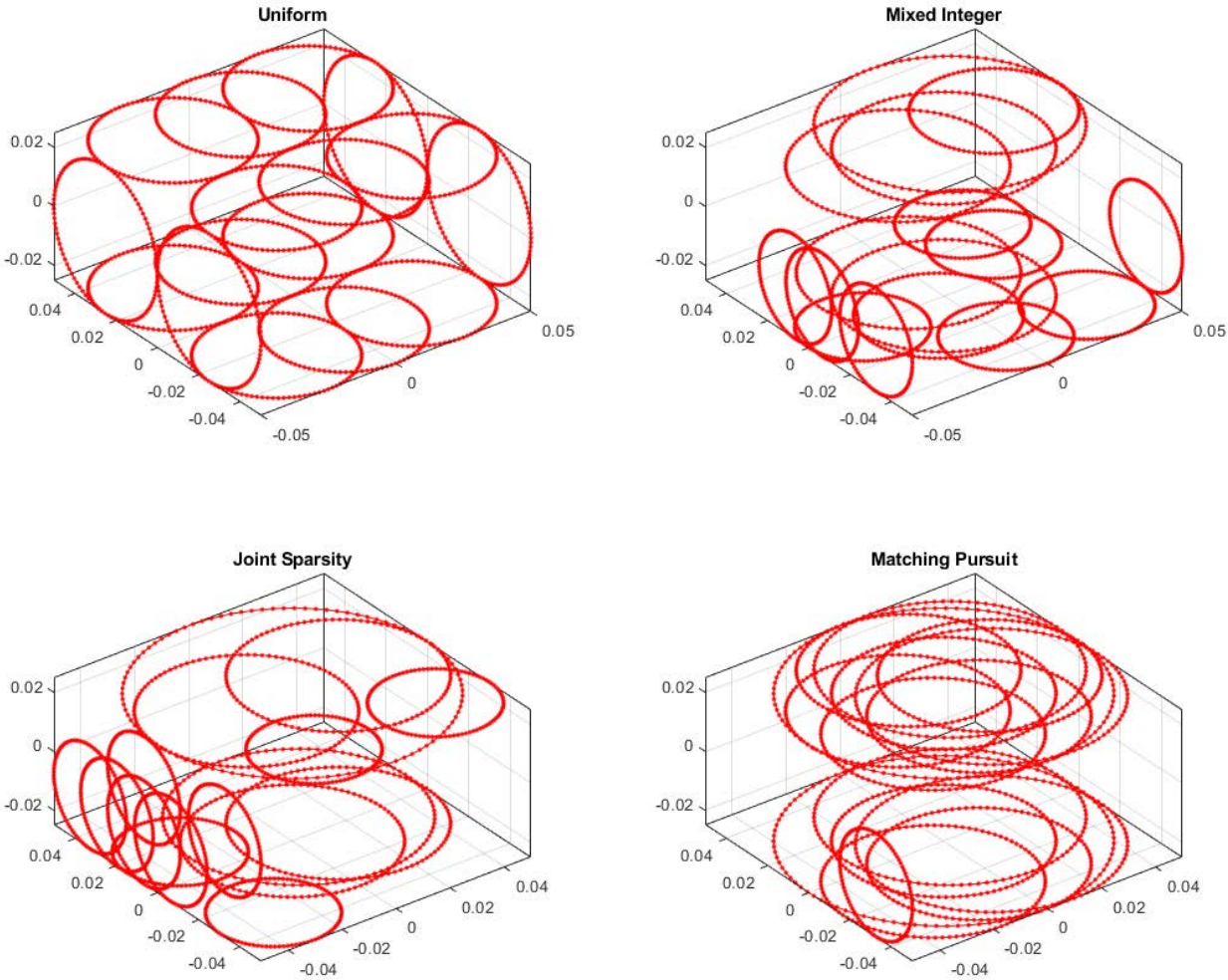
Figure 6.1: The coils selected by each of the above optimization algorithms. The top left depicts the uniform coils we implemented in the second iteration of our shim array. Both the mixed integer and joint sparsity optimization seem to favor similar areas that tend to have more inhomogeneities. The matching pursuit algorithm, however, seems to concentrate the coils only on the coronal faces.
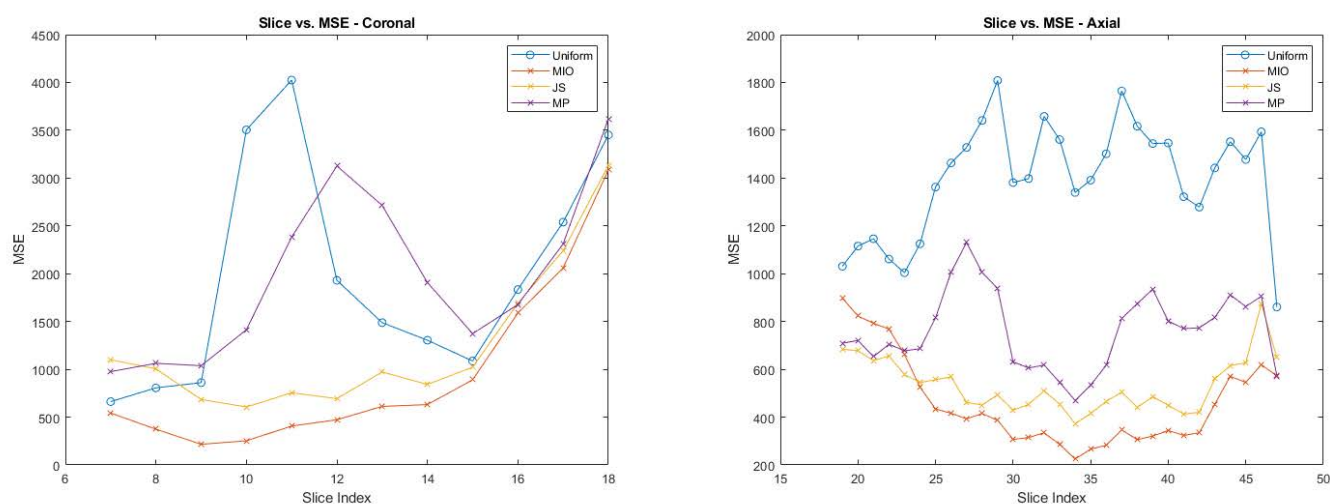
Figure 6.2: MSE plots of each algorithm. Because our algorithms are essentially minimizing the mean squared error (MSE), we plot the MSE of each optimization algorithm for every slice, both in the coronal and axial directions. While both the mixed integer and joint sparsity optimization algorithms perform much better than the uniform and matching pursuit algorithms in the coronal case, matching pursuit seems to improve in the axial direction. In both cases, the mixed integer algorithm yields the best results.

Chapter 7

Discussion

7.1 Conclusion

In this project, we presented a local B_0 shim array for permanent magnet scanners that could be placed close to the subject without coupling to the B_1 field. We also demonstrated that our targeted shimming reduced the overall field inhomogeneity for a individual slice by a factor of 3.

Our experimental setup utilized shim arrays that we constructed ourselves, as well as noise-minimizing, feedback-controlled printed circuit boards, and an automated process to acquire fieldmaps. Through our experimentation, we observe a significant increase in field homogeneity with minimal interference with the fundamental MR system.

7.2 Future Work

In this project, we have shown that the shim array we constructed is successful at correcting field inhomogeneities for targeted slices. Dynamic shimming, in which we sequentially shim every slice in a volume, would homogenize the magnetic field of the entire field of view. This requires quickly performing our least squares optimization and updating the current solutions before the next slice's fieldmap is calculated. While our current driver board system was designed for such a task, the scanner requires more hardware to interface with the Teensy and MATLAB sequencing. Namely, replacing the back of the scanner with a connector plate would allow for a trigger system in which the gradient signal is read by the Teensy and the amplifier boards are synchronized with the new current values. This would also allow for the wires to be connected to the back of the scanner, allowing for the subject to be more easily inserted.

As shown in the shim selection algorithm chapter, there are more optimal coil configura-

tions that can be designed to further reduce field inhomogeneity. These shim arrays require more precision than our previous shim array iterations, so possible construction methods can include copper etching or fabricating flex PCBs. Designing a new sleeve for the RF solenoid in CAD would also better accommodate various new shim array configurations.

The ultimate goal is to be able to use this shimming system on human subjects. While we demonstrated significant improvement on our bottle phantom, we hope that this system can be used to improve clinical permanent magnet scanners.

Bibliography

[1]   Hui Han et al. "Integrated parallel reception, excitation, and shimming (iPRES)". In: *Magnetic resonance in medicine* 70.1 (2013), pp. 241–247.

[2]   Shao Ying Huang et al. "Portable Low-cost MRI System based on Permanent Magnets/Magnet Arrays". In: (2018).

[3]   Nick Arango and Jason P Stockmann et al. "Open-source, low-cost, flexible, current feedback-controlled driver circuit for local B0 shim coils and other applications". In: *ISMRM* (2016).

[4]   Stephen P. Bradley, Arnoldo C. Hax, and Thomas L. Magnanti. *Applied Mathematical Programming*. Addison-Wesley, 1977, pp. 272–296.

[5]   C Juchem C and RA de Graaf. "B0 magnetic field homogeneity and shimming for in vivo magnetic resonance spectroscopy". In: *Analytical Biochemistry* 529 (2017), pp. 17–29. DOI: `10.1016/j.ab.2016.06.003`.

[6]   Galiana G et al. "The Role of Nonlinear Gradients in Parallel Imaging: A k-Space Based Analysis". In: *Concepts in Magnetic Resonance* 40A.5 (2012), pp. 253–267. DOI: `10.1002/cmr.a.21243`.

[7]   Yang Gao et al. "A 16-channel AC/DC array coil for anesthetized monkey whole-brain imaging at 7T". In: *NeuroImage* 207 (2020), pp. 116–396.

[8]   Douglas C. Giancoli. *Physics for Scientists and Engineers*. Englewood Cliffs, N.J.: Prentice Hall, 1989.

[9]   Michael Grant and Stephen Boyd. *CVX: Matlab software for disciplined convex programming, version 2.0*. 2013.

[10]   Michael Grant and Stephen Boyd. *Graph implementations for nonsmooth convex programs, Recent Advances in Learning and Control*. 2008.

[11]   Liming Hong and D. Zu. "Shimming Permanent Magnet of MRI Scanner". In: *Piers Online* 3 (2007), pp. 859–864.

[12]   Kevin M Koch et al. "Sample-specific diamagnetic and paramagnetic passive shimming". In: *JMRI* 182.1 (2006), pp. 66–74.

[13] Feng Liu et al. "A Hybrid Field-Harmonics Approach for Passive Shimming Design in MRI". In: *IEEE Transactions on Applied Superconductivity* 21.2 (2011), pp. 60–67. DOI: 10.1109/TASC.2011.2112358.

[14] José P. Marques, Frank F.J. Simonis, and Andrew G. Webb PhD. "Low field MRI: an MR Physics perspective". In: *JMRI* 49.6 (2019), pp. 1528–1542.

[15] Loic Queval. *BSmag toolbox user manual*. 2015.

[16] Jason P. Stockmann et al. "A 32-channel combined RF and B0 shim array for 3T brain imaging". In: *Magnetic Resonance in Medicine* 75.1 (Feb. 2015), pp. 441–451. DOI: 10.1002/mrm.25587. URL: https://doi.org/10.1002/mrm.25587.

[17] Sharon E. Ungersma et al. "Shim design using a linear programming algorithm". In: *Magnetic Resonance in Medicine* 52.3 (2004), pp. 619–627. DOI: 10.1002/mrm.20176. URL: https://doi.org/10.1002/mrm.20176.

[18] Peter T. While and Jan G. Korvink. "Designing MR Shim Arrays With Irregular Coil Geometry: Theoretical Considerations". In: *IEEE Transactions on Biomedical Engineering* 61.6 (2014), pp. 1614–1620. DOI: 10.1109/TBME.2013.2293842.

[19] JL Wilson, M Jenkinson, and P Jezzard. "Optimization of static field homogeneity in human brain using diamagnetic passive shims". In: *Magnetic Resonance in Medicine* 48.5 (2002), pp. 906–914. DOI: 10.1002/mrm.10298.